Strong-field ionization of water. II. Electronic and nuclear dynamics en route to double ionization

Chuan Cheng , ¹ Zachary L. Streeter, ^{2,3} Andrew J. Howard , ^{4,5} Michael Spanner, ^{6,7} Robert R. Lucchese, ² C. William McCurdy, ^{2,3} Thomas Weinacht, ¹ Philip H. Bucksbaum, ^{4,5,8} and Ruaridh Forbes , ^{4,8,9,*}

¹ Department of Physics, Stony Brook University, Stony Brook, New York 11794, USA

² Chemical Sciences Division, Lawrence Berkeley National Laboratory, Berkeley, California 94720, USA

³ Department of Chemistry, University of California, Davis, California 95616, USA

⁴ Stanford PULSE Institute, SLAC National Accelerator Laboratory, 2575 Sand Hill Road, Menlo Park, California 94025, USA

⁵ Department of Applied Physics, Stanford University, Stanford, California 94305, USA

⁶ National Research Council of Canada, 100 Sussex Drive, Ottawa, Ontario, Canada K1A 0R6

⁷ Department of Physics, University of Ottawa, Ottawa, Ontario, Canada K1N 6N5

⁸ Department of Physics, Stanford University, Stanford, California 94305, USA

⁹ Linac Coherent Light Source, SLAC National Accelerator Laboratory, Menlo Park, California 94025, USA



(Received 13 April 2021; accepted 22 July 2021; published 23 August 2021)

We investigate the role of nuclear motion and strong-field-induced electronic couplings during the double ionization of deuterated water using momentum-resolved coincidence spectroscopy. By examining the three-body dicationic dissociation channel, $D^+/D^+/O$, for both few- and multicycle laser pulses, strong evidence for intrapulse dynamics is observed. The extracted angle- and energy-resolved double ionization yields are compared to classical trajectory simulations of the dissociation dynamics occurring from different electronic states of the dication. In contrast to measurements of single-photon double ionization, pronounced departure from the expectations for vertical ionization is observed, even for pulses as short as 10 fs in duration. We outline numerous mechanisms by which the strong laser field can modify the nuclear wave function en route to final states of the dication where molecular fragmentation occurs. Specifically, we consider the possibility of a coordinate dependence on the strong-field ionization rate, intermediate nuclear motion in monocation states prior to double ionization, and near-resonant laser-induced dipole couplings in the ion. These results highlight the fact that, for small and light molecules such as D_2O , a vertical-transition treatment of the ionization dynamics is not sufficient to reproduce the features seen experimentally in the strong-field coincidence double-ionization data.

DOI: 10.1103/PhysRevA.104.023108

I. INTRODUCTION

Investigations into the mechanisms of strong-field ionization (SFI) remain an important cornerstone in ultrafast science research due to its central role in strong-field-induced phenomena such as high-harmonic generation [1–3], laser-induced electron diffraction [4–6], and Coulomb-explosion imaging [7,8]. SFI has also been used as a "pump" for experiments that aim to study charge transfer or charge migration in molecular cations [9–12]. For molecular systems this continued interest is in part due to the complexity of the SFI process when compared with atomic systems [13,14]. Critical differences that are partially responsible for this are the spatial arrangement of the nuclei that give rise to the molecular structure; the presence of internal degrees of freedom, vibrations, and rotations; and the significantly higher density of electronic states that are typically found in these systems [15,16].

For many experiments, the ideal scenario is that SFI serves as a "sudden" transition, where the nuclei do not move during the pulse that induces the ionization [17–19]. The electron rearrangement that accompanies sudden transitions can be compared to the "vertical" transitions that describe weak-field

perturbative ionization, where a portion of the ground-state vibrational wave function is projected onto the electronic states of the mono- or dication. The notion of a vertical transition is based on the idea that the transition dipole moment for the coupling of two electronic states by a weak (perturbative) external field is roughly independent of the nuclear coordinate over the extent of the initial wave function. This allows one to factor the coupling matrix element into an electronic term which is multiplied by an overlap of the initial vibrational wave function with the vibrational eigenstates of the upper electronic state, and thus, the initial vibrational wave function is simply "vertically lifted" and projected (mapped) onto the excited-state potential-energy surface (PES). This assumption is frequently described in terms of the Franck-Condon principle [20].

Nuclear motion during the pulse is not the only mechanism for nonvertical ionization. Coordinate-dependent strong-field ionization rates [21,22] and impulsive Raman excitation in one of the electronic states could also result in deviations from vertical ionization [23,24].

Recent work that considered the single-photon double ionization of water showed excellent agreement between the measured and calculated momentum-resolved yield of fragment ions assuming vertical ionization [25,26]. Here we explore the extent to which SFI with short pulses can be

^{*}ruforbes@stanford.edu

considered vertical. Using a combination of coincidence velocity-map imaging of fragment ions and trajectory calculations for the three-body dissociation dynamics of the molecular dication, we demonstrate that even for very short pulses (<10 fs), the ionization cannot be considered to be "vertical" but involves reshaping (changes to the first and second moments of the distribution) of the vibrational wave function during the ionization dynamics. We discuss different contributions to the wave-function reshaping during ionization.

Our measurements, calculations, and analysis may help interpret previous work that made use of SFI as probe of excited-state dynamics [27-29] and for vibrational wavepacket holography [30]. In the case of probing excited-state dynamics, while SFI produced qualitatively similar timedependent yields as weak-field or single-photon ionization, quantitative agreement was not possible [27]. We argue that this lack of agreement is due to variation in SFI rates with nuclear geometry and reshaping of the vibrational wave packet during SFI. While the holography measurements showed very nice agreement between the experiment and theory in terms of the interference fringe positions and visibility, details of the comparison were not perfect due to the limited ion-imaging ability and the assumption of vertical ionization. Our work directly examines this assumption and can be thought of as characterizing the instrument response function associated with SFI as a probe. Particularly for early time delays in pump-probe experiments, where the initial and final PESs vary significantly with the nuclear coordinate, SFI can differ from vertical ionization significantly. Also, for high intensities, one can see enhancement of ionization to higher charge states through charge-resonance-enhanced ionization, which also violates the notion of vertical ionization [31,32]. Finally, for pulses longer than 10 fs, experiments and simulations are greatly affected by laser-induced dynamic alignments and couplings between different electronic states [33–36].

In terms of theoretical investigations into the SFI dynamics of water, recent frozen-nuclei time-dependent R-matrix ab initio ionization computations on H₂O [37] suggested that laser coupling in the ion can significantly modify the angular dependence of the ionization dynamics when using multicycle pulses. However, if intermediate motion takes place on the ionic surface, adding the laser coupling during the ionizing pulse without also including nuclear motion on the laser-coupled ionic states becomes suspect. Motion on the ionic states will affect the phases and populations on each laser-coupled surface, which can, in turn, affect the ionization dynamics. The current alternative approach to modeling ionization in multicycle strong fields when motion in the ion states is present can be seen in studies of N₂⁺ lasing, where the strategy is to compute half-cycle ionization yields which are then used as inputs into separate laser-coupled ion-dynamics computations [38,39]. This is the approach that we adopt in the present paper—our half-cycle ionization yields were presented in a previous paper [36], and herein we carry out the laser-driven ionic dynamics. A more rigorous treatment could involve adding the ionization contributions from different half cycles to the laser-coupled ion-dynamics simulation through inclusion of a source term in a density-matrix approach [40].

II. EXPERIMENT

Two similar apparatuses were used to carry out the measurements. Since they are almost the same, we provide a description of the apparatus used to carry out the 10-fs pulse measurements (described in detail in previous work [41,42]) and indicate any differences for the apparatus used for the 40fs pulse measurements. Briefly, the output from a commercial amplified Ti:sapphire laser system (1 mJ, 780 nm, 1 kHz) is spectrally broadened using filamentation in Ar gas and compressed to ~10 fs using chirped mirrors and an acoustooptic pulse shaper [43]. The laser pulses are directed into a vacuum chamber (base pressure of 10^{-10} mbar) and focused at the center of a velocity-map imaging (VMI) spectrometer using an in-vacuum concave silver mirror (f = 5 cm). The in situ intensity was calibrated by SFI of argon, measuring the classical $2U_p$ cutoff for field-ionized electrons from argon [44] at low pulse energies and extrapolating to higher ones (using a procedure outlined in Ref. [45] for the 40-fs measurements). The estimated intensities for the 10- and 40-fs measurements are 400 and 600 TW/cm², respectively.

Target D_2O molecules are expanded into a separate source chamber and subsequently skimmed to yield an effusive molecular beam [41]. This beam intersects the focused laser at the center of the electrostatic lens stack of the VMI spectrometer [41]. The extracted ions and electrons are recorded using a microchannel plate, phosphor screen, and Timepix3 camera with 1.5-ns time resolution (a RoentDek hexanode detector, with a time resolution of <1 ns [46], was used for the 40-fs pulse measurements).

In order to ensure the low count rates required for coincident detection of all charged particles, a working pressure of 4×10^{-10} Torr was used throughout the experiment (with a base pressure of about 1×10^{-10} Torr). The adopted pressure resulted in an average event rate of approximately 0.8 per laser shot, which in turn corresponded to an event rate of <0.1 per shot for the double-ionization channels considered in this work. Presented in Table I are the experimentally extracted yields and branching ratios for the dissociation channels following strong-field double ionization. Two-body fragmentation into OD⁺/D⁺ is the dominant channel, followed by three-body fragmentations into $D^+/D^+/O$ and $D^+/D/O^+$. In the present work we focus our discussion on the three-body $D^+/D^+/O$ fragmentation channel. A detailed analysis of fragmentation into OD⁺/D⁺ was included in an earlier publication, which investigated the roles of dynamic and geometric alignment during water double ionization [34]. We note that our extracted ratios differ significantly in some channels from reported values for single-

TABLE I. Branching ratios of relevant water dication dissociation channels. The detection efficiencies of different ions are estimated to be $0.58 \, (D^+)$, $0.2 \, (O^+)$, and $0.3 \, (OD^+)$.

Channels	Counts: uncorrected	Efficiency: uncorrected	Counts: corrected	Efficiency: corrected
$\begin{array}{c} \hline \\ D^{+}/OD^{+} \\ D^{+}/D^{+}/O \\ D^{+}/O^{+}/D \\ \end{array}$	6.5×10^4	0.632	3.7×10^5	0.702
	3.0×10^4	0.288	8.8×10^4	0.165
	8.2×10^3	0.080	7.0×10^4	0.133

TABLE II. Electronic states of the water dication in different conventions. Branching ratios are for the dissociation dynamics on the *ab initio* potential surfaces with initial conditions from the Wigner phase-space distribution of the ground vibrational state, calculated from 10⁵ trajectories on each potential surface, similar to the calculations in [25,26].

C _s symmetry	Spin-state order	$C_{2\nu}$ symmetry	$C_{2\nu}$ configuration	Two-body branching ratio (%)	Three-body branching ratio (%)
$\overline{X^3A''}$	T_0	$^{3}B_{1}$	$(3a_11b_1)^{-1}$	92	8
$2^{3}A''$	T_1	$^{3}A_{2}$	$(1b_21b_1)^{-1}$	0	100
$1{}^{3}A'$	T_3	$^{3}B_{2}$	$(1b_23a_1)^{-1}$	0	100
$1 {}^{1}A'$	S_0	$1 {}^{1}A_{1}$	$(1b_1)^{-2}$	100	0
$1 {}^{1}A^{"}$	S_1	$^{1}B_{1}$	$(3a_11b_1)^{-1}$	87	13
$2^{1}A'$	S_2	$2^{1}A_{1}$	$(3a_1)^{-2}$	26	74
$2^{1}A''$	S_3	$^{1}A_{2}$	$(1b_21b_1)^{-1}$	0	100
$3^{1}A'$	S_4	$^{1}B_{2}$	$(1b_23a_1)^{-1}$	0	100
$3^{1}A''$	S_5	$3^{1}A_{1}$	$(1b_2)^{-2}$	0	100

photon double ionization [47] and, more critically, SFI with higher-intensity longer-duration pulses [48]. Furthermore, we note the absence of the weak D_2^+/O^+ channel observed in Ref. [48] in our data recorded with 10-fs pulses. A detailed investigation into the pulse-duration dependence of double-ionization branching ratios is beyond the scope of the present work.

III. TRAJECTORY CALCULATIONS

Classical trajectory calculations simulate the conditions of single-photon double ionization of the ground state of D₂O in which the molecule undergoes a Franck-Condon transition to the doubly ionized excited state. The trajectories are propagated on the field-free potential surfaces of the lowest nine states of the water dication. Those states are created, in the simple molecular-orbital picture, by removing two electrons in all possible ways from the three highest filled molecular orbitals of the neutral, as indicated in Table II, leaving the D_2O^{++} ion in all possible spin states for each configuration. The surfaces were calculated earlier [25,49] with MOLPRO [50,51] using internally contracted multireference configuration interaction (icMRCI) methods at the configuration interaction (CISD) singles and doubles level, including the Davidson correction to the quadruple excitations energy. The full-dimensional surfaces were then fitted using a functional form which is a fit (linear least squares) to an accurate form involving 100 basis functions developed by Gervais et al. [49].

The trajectory calculations assumed the neutral water molecule is initially in its ground vibrational state with zero total rotational angular momentum. The initial conditions for 10^5 trajectories on each potential surface were sampled from the Wigner phase-space distribution for the computed normal modes of the ground electronic state in icMRCI calculations. The phase-space distribution has the form

$$W(\mathbf{Q}, \mathbf{P}) = \frac{1}{(\pi \hbar)^{3N-6}} \prod_{j=1}^{3N-6} e^{-\frac{\omega_j}{\hbar} Q_j^2 - \frac{1}{\hbar \omega_j} P_j^2},$$
(1)

where N is the number of atoms, w_j are the associated frequencies, and the vectors \mathbf{Q} and \mathbf{P} are the normal-mode

coordinates and momenta, respectively, and are positive definite for the case of the ground state. A similar trajectory study was performed for double ionization of H₂O previously [25] and compared extensively with experimental momentum images [26] from single-photon double-ionization measurements using the cold-target recoil-ion-momentum spectroscopy technique [52–54]. That comparison validated the accuracy of this *ab initio* treatment of the dissociation of the cation in all but its finest details. The present calculations differ only in the masses of the atoms (D versus H) and the larger number of trajectories on each surface (10⁵ versus 10³). They thus show small quantitative differences from the previous work, for example, in the two-body versus three-body dissociation branching ratios.

Classical trajectory calculations with nonzero initial rotational angular momentum which is in the range of angular momenta thermally populated in a supersonic expansion were performed. This additional rotational degree of freedom produces negligible differences from the final momentum distributions of the atomic fragments computed with zero total angular momentum. Further, the importance of rotational dynamics of molecules in the context of strong-field ionization was investigated in an earlier publication [34].

The potential-energy curves along the symmetric stretch coordinate of the first nine states of dication are shown in Fig. 1. The state characters are labeled according to $C_{2\nu}$ symmetry. Outlined in Table II are the equivalent labeling conventions in other symmetries, together with the dominant electronic configurations for these states near the equilibrium geometry of the neutral molecule and the associated two- and three-body theoretical branching ratios for the present case of D₂O. The criterion for categorizing a trajectory as three body in this work was that the $R_{\rm OD}$ distance of one deuterium be 200 bohrs or greater and that the other reach at least 50 bohrs. The long distances used for the criterion to separate two-body from three-body dissociation channels are chosen because the diatomic fragments can be produced with vibrational excitation near their dissociation limits. High vibrational and rotational excitation in the products produced by dynamics on several of the potential surfaces is discussed in [49], which computed the internal energy distributions of the diatomic fragments in

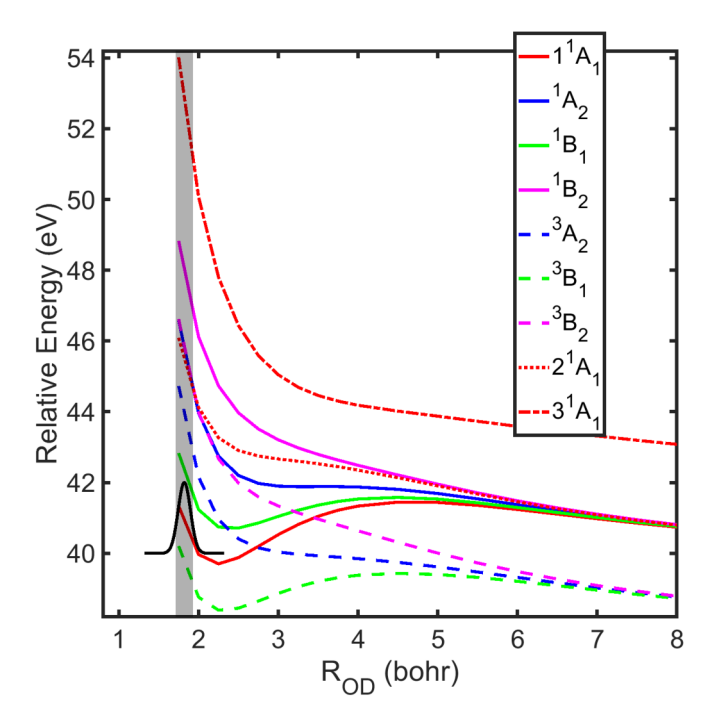


FIG. 1. Potential-energy curves for the first nine states of the D_2O dication as a function of the symmetric stretch coordinate R_{OD} , together with the neutral ground-state wave function (solid black line). The vertical shaded gray line illustrates the extent of the ground-state wave function. The curves included here are reproduced from Ref. [25].

the two-body channels. In other words, it is a long propagation time (1.5 ps in this simulation) for three-body dissociation but not long enough for the sequential break up. Moreover, the $D^+/O^+/D$ channels are spin forbidden from the initial populated states unless the molecule goes through a nonadiabatic transition in the sequential process which is not included in the present simulations but further discussed in [25,49].

IV. MEASUREMENTS

Given the agreement between the trajectory calculations and the single-photon double-ionization measurements described above, the question we address here is whether strong-field double ionization prepares a similar superposition of states of the dication and whether the wave packet launched on each state via SFI is similar to the one launched by singlephoton (weak-field) ionization; that is, can the SFI process be thought of as vertical? We therefore compare the calculated double-ionization yield as a function of final angle between D^+/D^+ ions, β , and kinetic-energy release (KER) with our measurements. Figure 2 shows the measured and calculated $D^+/D^+/O$ yield (β -KER plot). Figure 2(a) shows the measured yield as a function of β and KER. Figure 2(b) shows the calculated yield vs β and KER assuming vertical ionization with equal population of the dication states. Figure 2(c) shows the same results as Fig. 2(b) with coefficients for the first nine states of the dication fitted to achieve the best agreement with the measurements. Figure 2(d) shows the calculated results accounting for experimental broadening of the features due

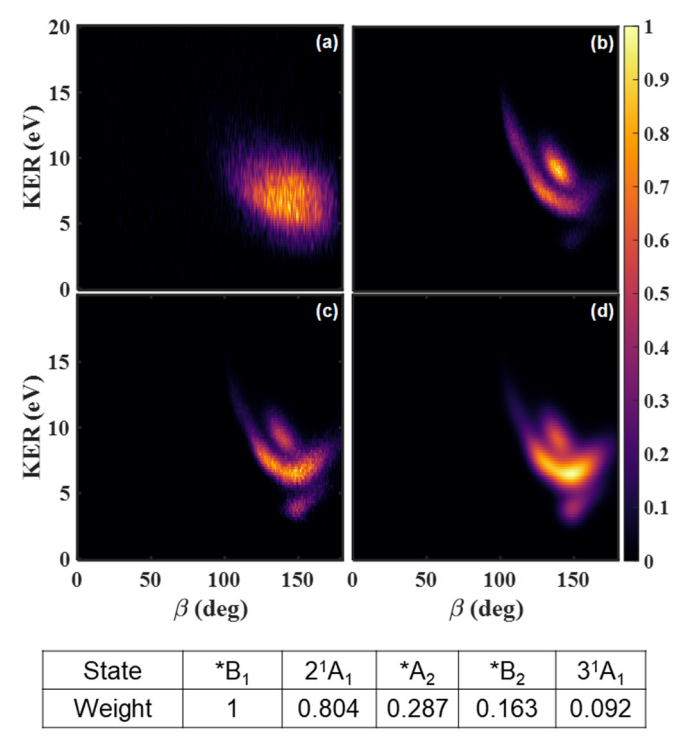


FIG. 2. Measured and calculated $D^+/D^+/O$ yield as a function of angle between the two D^+ ions' momentum β and the kineticenergy release (KER). (a) Measured coincidence $D^+/D^+/O$ yield as a function of β and KER for laser parameters described in the text. (b) Simulated $D^+/D^+/O$ yield as a function of β and KER for equal population of each of the first nine states of the dication. (c) Simulation of β -KER with fit and (d) simulation of β -KER with experimental resolution included. The table at the bottom lists the relative fitting populations for each state where the states are labeled with their $C_{2\nu}$ symmetry due to the lack of spin information in the observable. Details are outlined in the text.

to the limited resolution of our VMI apparatus, the details of which are discussed below.

In the fitting procedure, due to the lack of the spin-state information about the oxygen atom, states of the same $C_{2\nu}$ symmetry (e.g., ${}^{1}B_{1}$ and ${}^{3}B_{1}$) are grouped together since they are not separable in the β -KER plot [25]. From now on we just use the word "state" to represent different $C_{2\nu}$ symmetries. As can be seen from Fig. 9, each state populates a distinct region ("island") of the β -KER plot. More details on the island assignments can be found in Refs. [25,26] as well as in Appendix A. Based on these islands, a simple principle component analysis (PCA) procedure that minimizes the residual was used to reproduce the β -KER plot. The Population of different states have been fitted, and the reconstructed β -KER plot is shown in Fig. 2(c). The fitted relative state populations are listed in the table in Fig. 2 as well. The coefficients from the fit decrease with increasing ionization potential, roughly in agreement with expectations from the simple quasistatic tunnel-ionization model of Ammosov, Delone, and Krainov (ADK theory [55]). An interesting observation is that while the relative weights of states that involve removing electrons from different orbitals are in reasonable agreement with predictions from ADK theory, the relative weights of singlet

states that involve removing two electrons from the same orbital with opposite spins are significantly higher than predictions based on ADK theory. This observation may indicate cooperative behavior or nonsequential double ionization to states of the dication that involve removing two electrons from the same orbital.

The fitting in Fig. 2(c) only coarsely matches the measurements shown in Fig. 2(a). Although the experimental yield shows a center of mass similar to the calculations, the distinct state-resolved features in the β -KER plot are not captured in the SFI results. An important first check that we carried out in addressing this discrepancy is to determine whether our experimental resolution broadens the features such that they are no longer resolved. Using the coincidence events from the two-body dissociation channel (D^+/OD^+) , we obtained an uncertainty for the measured D⁺ momentum of 2.7 a.u. by checking the nature of momentum conservation in all three dimensions $(p_x, p_y, \text{ and } p_z)$. The energy of each D⁺ ion in the three-body channel is about 4.5 eV. Thus, the uncertainty of kinetic energy release (KER) $E_{\rm KER}$ is calculated to be $\delta E_{\rm KER} = \sqrt{2} p \delta p/m = 0.99 \, {\rm eV}$. Similarly, one can obtain the uncertainty of the angle between the two D+ momenta to be $\delta\beta = \sqrt{2\delta p/p} = 0.109 \,\mathrm{rad}.$

Applying the PCA, together with the experimental resolution correction, yields Fig. 2(d). The agreement between theory and experiment is still relatively poor: Notably, the islands corresponding to the $^{1}B_{1}$ and $^{3}B_{1}$ states are absent in the measurements (see Appendix A). In Fig. 2(d), where the states are blurred according to our instrument response function, the state island features are still present. This is at odds with the experimental yield shown in Fig. 2(a), where no separate features are present. Thus, we conclude that there has to be some mechanism that drives the difference between simulation and the experiment. We note that this disagreement between experiment and theory is independent of exactly what representation one chooses (i.e., which observables one looks at), and a number of different data representations are shown in Appendix B.

V. DYNAMICS CALCULATIONS AND DISCUSSION

The calculated and measured β -KER plots show some rough agreement but disagree on many details, so it is natural to ask whether the discrepancies could be due to dynamics occurring during the SFI process. In particular, we consider the role of wave-packet reshaping (due to coordinate-dependent ionization rates, for example) and nuclear dynamics (such as bending or rotation). As a first test of how much displacement the wave packet would need to alter the β -KER plot, we mapped the correlation between initial and final values for the distribution of sample points used in the classical trajectory calculations. As the dynamics calculations include an ensemble of initial and final coordinate values, we can plot the final values as a function of the initial ones, allowing us to see if there are correlations between them that lead the strong-field reshaping of the ground-state wave function to smear out the features in the measured β -KER plot.

Based on the simulation, we constructed the correlation maps shown in Fig. 3. Presented are correlation maps for three different electronic states, illustrating the correlation between

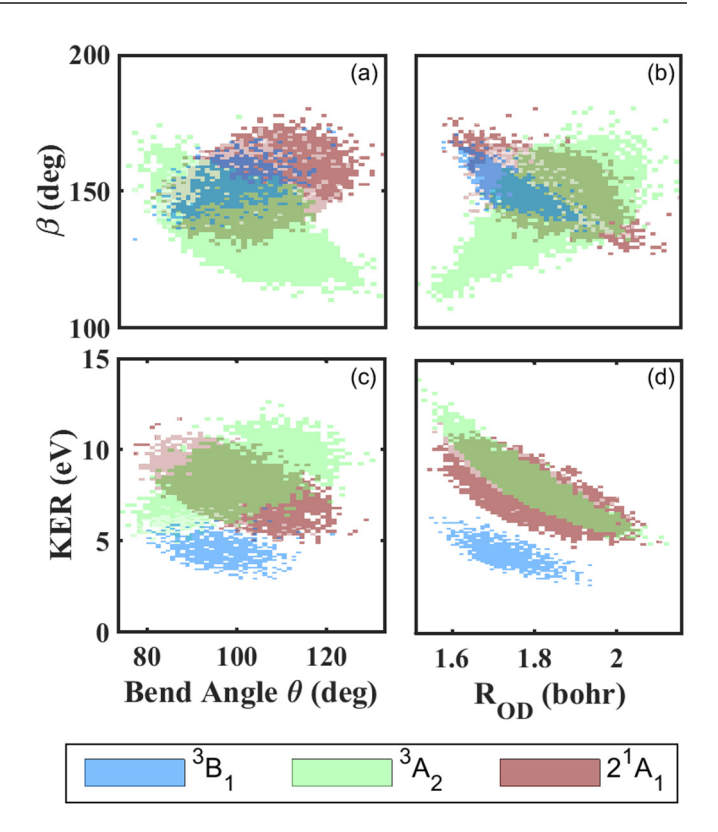


FIG. 3. Calculated D⁺/D⁺/O yield as a function of KER, β , and initial O-D separation or D-O-D bend angle θ for three states: 3B_1 [blue (medium gray) shading], 3A_2 [green (light gray) shading] and 2^1A_1 [red (dark gray) shading)]. (a) The D⁺/D⁺/O yield as a function of initial D-O-D angle and β . (b) The D⁺/D⁺/O yield as a function of initial O-D distance and β . (c) The D⁺/D⁺/O yield as a function of initial D-O-D angle and final KER. (d) The D⁺/D⁺/O yield as a function of initial O-D distance and final KER. The color coding here is consistent with Fig. 9.

the initial opening angle and symmetric stretch coordinate with respect to the β and KER. The correlation between the initial symmetric stretch coordinate $R_{\rm OD}$ and β and KER or the initial D-O-D angle and β and KER is a result of the finite width of the initial wave function and the nonzero slope of the dicationic PES at the Franck-Condon location.

Figures 3(a) and 3(b), which show how the β values depend on the initial coordinates, exhibit a strong state dependence. The ${}^{3}B_{1}$ and $2\,{}^{1}A_{1}$ states show a positive correlation between the β value and the initial opening angle, while the ${}^{3}A_{2}$ state shows a negative correlation. The behavior with respect to the initial O-D distance is the opposite. This illustrates how reshaping or the motion of the initial ground-state wave function can result in β distributions different from those predicted for single-photon ionization. Figures 3(c) and 3(d) show the KER dependence on the initial coordinates. Again, there is a significant dependence of the KER on the initial bend angle and O-D distance, illustrating how reshaping or the motion of the initial ground-state wave function can distort the KER distributions predicted for single-photon ionization. These plots motivate an examination of the different strongfield mechanisms that can result in nonvertical ionization and the measured β -KER plots. The sensitivity of the correlation between initial and final coordinates of the electronic state is

related to the breakdown of the axial recoil approximation and "slingshot" motion of the D⁺ ions for the ${}^{3}B_{1}$ and 2 ${}^{1}A_{1}$ states, as discussed in more detail in [25].

The calculated β -KER plots shown in Figs. 2(b) and 9 are the result of applying one-photon perturbation theory to describe the transition from the initial neutral directly into the dication states, which is then followed by classical propagation to compute the final fragment energies and angles. In this treatment, the initial Wigner function launched on the dication states is then simply the Wigner function corresponding to the normal-mode ground state of the neutral species, that is, the Franck-Condon wave packet. While this treatment is applicable to weak-field ionization in which one-photon perturbation theory is applicable, additional effects are present during SFI that modify the initial neutral ground-state wave packet before it arrives at the dication surfaces. First, the SFI rate can depend strongly on the nuclear coordinates, an effect which can reshape the initial ground-state nuclear wave packet during ionization. Second, multiple ionization via SFI is typically a sequential process in which there is a time delay between the ejection of each liberated electron, thereby giving the nuclei a chance to relax and rearrange between different ionization events. Finally, since there is still a strong-field present during this time delay, near-resonant laser-driven electronic transitions can occur, causing additional nonionizing electronic transitions that reshape the nuclear wave packets while the molecule is in an intermediate ionic state.

We now outline each of these effects in more detail. We do not attempt a complete treatment of D_2O double ionization in strong fields with all degrees of freedom active, which, although desirable, represents a massive theoretical and computational task. Rather, we limit ourselves to outlining each effect using simplified reduced-dimensionality models. Since ionization to both the X and A cation states is expected to occur [36], modifications and dynamics arising from ionization to both X and A are used to exemplify these effects.

Coordinate-dependence of the SFI rate. SFI with low-frequency fields can be envisioned as a quasistatic tunnel-ionization process in which the ionization rate depends exponentially on the ionization potential (IP) through the Keldysh tunneling rate $\Gamma(\mathbf{R},t)$ [21,56–58]. In this description, ionization occurs in short subcycle bursts near the peaks of the laser oscillations. With the assumption that the nuclei remain stationary during a single-ionization burst, the ionized wave packet after the burst can be written as

$$\Psi_K(\mathbf{R}) = \Gamma(\mathbf{R}, t)\Psi_0(\mathbf{R}), \tag{2}$$

where $\Psi_0(\mathbf{R})$ is the initial nuclear wave packet before ionization and \mathbf{R} stands for all nuclear coordinates. If ionized from the neutral at equilibrium, $\Psi_0(\mathbf{R})$ is often called the Franck-Condon wave packet. The Keldysh rate is given by

$$\Gamma(\mathbf{R},t) = \mathcal{P} \exp\left[-\frac{2}{3} \frac{[2 I_{P}(\mathbf{R})]^{3/2}}{|F(t)|}\right],\tag{3}$$

where \mathcal{P} is a slowly varying (i.e., nonexponential) prefactor that depends weakly on the IP I_P , F, and \mathbf{R} . Here F denotes the amplitude of the electric field. In molecular systems, the \mathcal{P} prefactor would also encode the molecular orientation dependence of SFI as well as other molecular effects such as

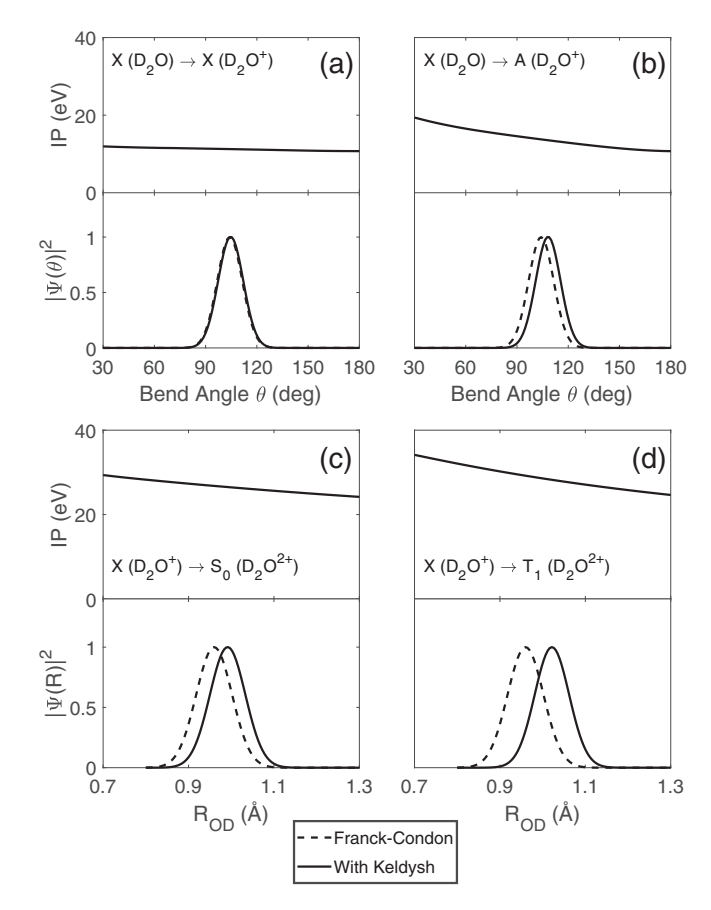


FIG. 4. Modification of the nuclear wave packet due to the coordinate-dependent Keldysh ionization rate. (a) and (b) The effect of the Keldysh weighing on the bending coordinate during the single-ionization event for both the X and A cation states. These panels plot the ionization potentials (IPs) for the transitions in question, the unmodified initial neutral (i.e., Franck-Condon) wave packet, and the nuclear wave packet after applying the Keldysh weighting. (c) and (d) The effects of the Keldysh weighting for two examples of single-to-double ionizing transitions (indicated in the panels) as a function of $R_{\rm OD}$, the bond length of the symmetric stretch mode. All probability densities $|\Psi|^2$ have been normalized to have a maximum of 1

enhanced ionization, and accurate computation of \mathcal{P} would require some form of *ab initio* numerical simulation of the ionization process. In the following we set $\mathcal{P}=1$ for simplicity and consider only the effects of the Keldysh exponent. Equation (2) shows that the Keldysh rate can modify the spatial structure of the Franck-Condon wave packet through the coordinate dependence of the IP.

Figure 4 shows examples of the Keldysh rate modifying the initial Franck-Condon wave packet in D_2O . Figure 4(a) shows the IPs for the first ionization step from the neutral to the X state of the ion along the bend coordinate θ together with cuts through the nuclear wave function both with and without applying the Keldysh weighting. Figure 4(b) plots the same thing but for the neutral to A state. While very little change in the wave function occurs for X ionization along this coordinate, it can be seen that the Keldysh weighting has the effect of shifting the Franck-Condon wave packet for the A state. Figures 4(c) and 4(d) plot similar cuts for two transitions

of the second ionization steps, $X \to 1^1 A_1$ (S_0) and $X \to {}^3 A_2$ (T_1), but now taken along the symmetric stretch coordinate. Due to the increased magnitude and steep coordinate dependence of the IPs for these transitions, the Keldysh-induced shifts of the wave function are more pronounced than the previous single-ionization examples.

Few-cycle nuclear motion in the ion. Following the first ionization event, the nuclear wave packet can begin to move on the cationic surfaces before the second ionization occurs. This intermediate motion can change the nuclear wave packets before being projected onto the dicationic states. From our investigations of the cationic surfaces, the dominant motion is expected to be along the bend coordinate. In reality the motion in the cation occurs in the presence of the laser field, but we first consider the effects of field-free motion, which alone can cause pronounced reshaping of the wave packets. Laser-driven motion in the cation is considered below.

The bending wave-packet dynamics on the X^2B_1 and A^2A_1 cationic surfaces is simulated using the following simplified model of D_2O^+ . First, the bond lengths are fixed at the neutral equilibrium values R_{eq} throughout the dynamics. Second, the bending is restricted to a single plane of motion, where the overall rotational motion about the center of mass is not considered during this wave-packet simulation. Finally, the mass of the oxygen atom is assumed to be infinite, which significantly simplifies the corresponding kinetic-energy operator. With these restrictions, the Hamiltonian of the model system is written (in atomic units) as

$$\widehat{H}(\theta,t) = \begin{bmatrix} -\frac{1}{2\mu R_{eq}^2} \frac{\partial^2}{\partial \theta^2} + V_X(\theta) & 0\\ 0 & -\frac{1}{2\mu R_{eq}^2} \frac{\partial^2}{\partial \theta^2} + V_A(\theta) \end{bmatrix},$$
(4

where $\mu = m_D/2$ is the reduced mass of the bend coordinate, m_D is the mass of atomic deuterium, and $V_X(\theta)$ and $V_A(\theta)$ are the potential-energy surfaces of the X^2B_1 and A^2A_1 states. This Hamiltonian is used to solve the time-dependent Schrödinger equation (TDSE) $i\partial_t \Psi(\theta,t) = \widehat{H}(\theta,t)\Psi(\theta,t)$. In order to investigate the effect of wave-packet motion separate from the Keldysh effects discussed above, we populate both the X and A surfaces during the ionization event starting from the unchanged Franck-Condon wave packet, and hence, the initial condition for $\Psi(\theta,t)$ at the moment of ionization is taken to be the bending ground state $\psi_0(\theta)$ on the neutral surface. The TDSE is solved using the Fourier-split-operator technique [59].

Figures 5(a)–5(c) show the effects of intermediate field-free few-cycle motion on the X and A cation surfaces. Figure 5(a) shows the Wigner function of the initial Franck-Condon wave packet. It is the initial state of the bending coordinate that is used in the β -KER trajectory simulations. Figures 5(b) and 5(c) plot Wigner functions after this initial state has propagated field free for a time corresponding to two laser cycles of the 780-nm field $(2 \times 2.6 \text{ fs})$ on the X and A states, respectively. The X-state Wigner has undergone a little acceleration and motion, as can be seen by the small shift of the center of the Wigner function, but there is still significant overlap between the propagated and initial Wigner functions in this case. However, the two-cycle field-free propagation on

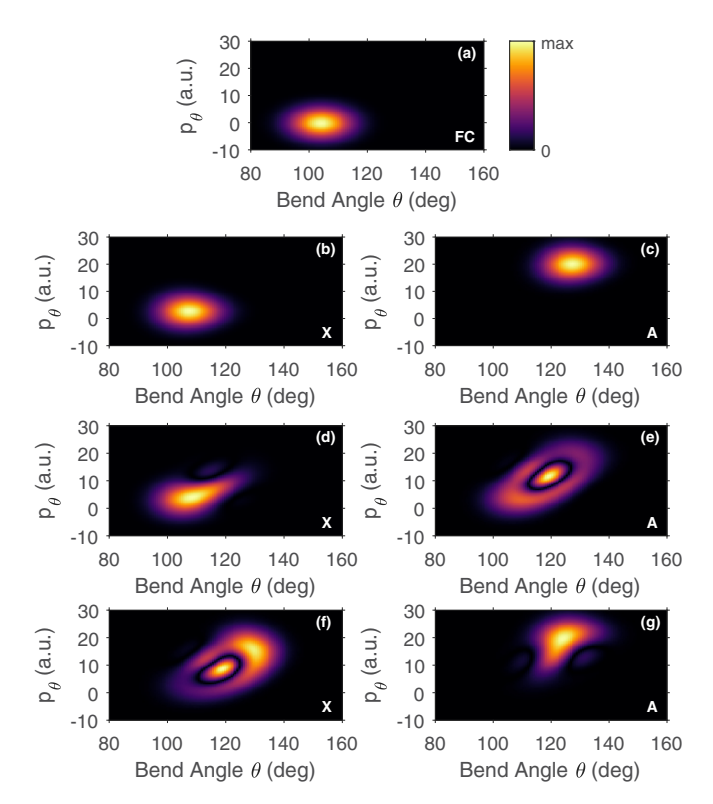


FIG. 5. Wigner functions demonstrating the effects of nuclear dynamics in the cation. (a) Wigner function of the Franck-Condon wave packet. (b) and (c) Wigner functions after field-free propagation on the X and A states, respectively, for a time equal to two cycles of the laser. (d) and (e) Wigner functions on the X and A states after laser-driven propagation for a time of two laser cycles with the initial population starting on the X state. The simulation was started at the peak of the pulse (t=0) with the laser parameter $\lambda_0=780$ nm, $I_0=400$ TW/cm², and $\tau=10$ fs. (f) and (g) The same as (d) and (e), but now with the initial population on the A state. Note that in all cases the magnitude of the Wigner function is shown.

the *A* state substantially modifies the initial Wigner function, which now has effectively zero overlap with the initial state. Figures 5(d)–5(g) pertain to laser-driven motion in the ion, which is outlined in the following.

Near-resonant dipole coupling in the ion. At 780 nm, the laser induces a near-resonance one-photon coupling between the *X* and *A* states. This coupling is included in the wave-packet simulation by adding off-diagonal dipole terms to the Hamiltonian, which then becomes

$$\widehat{H}(\theta,t) = \begin{bmatrix} -\frac{1}{2\mu R_{eq}^2} \frac{\partial^2}{\partial \theta^2} + V_X(\theta) & -F(t)d_{XA}(\theta) \\ -F(t)d_{XA}(\theta) & -\frac{1}{2\mu R_{eq}^2} \frac{\partial^2}{\partial \theta^2} + V_A(\theta) \end{bmatrix},$$
(5)

where $d_{XA}(\theta)$ is the transition dipole between these states and F(t) is the electric field of the laser which is chosen to be parallel to $d_{XA}(\theta)$, i.e., perpendicular to the molecular plane. The electric field of the laser is taken to have a Gaussian envelope

$$F(t) = \mathcal{F}_0 \exp\left[-4\ln 2\left(\frac{t}{\tau\sqrt{2}}\right)^2\right] \cos(\omega_0 t), \qquad (6)$$

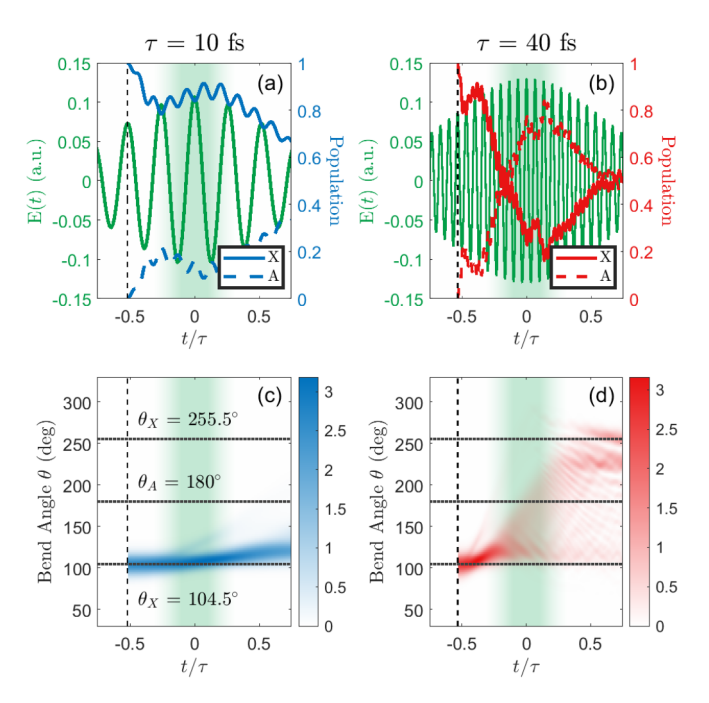


FIG. 6. Time-resolved simulations of the strong-field coupling between the X state of the water cation and the A state in the presence of (a) the 10-fs pulse with $\lambda_0 = 780$ nm and $I_0 = 400$ TW/cm² and (b) the 40-fs pulse with central wavelength $\lambda_0 = 800$ nm and peak intensity $I_0 = 600 \text{ TW/cm}^2$ (parameters are chosen to match the experiments). In each case, the cation is initiated in the X state (red and blue solid lines) at a local peak in electric field (solid green line) that roughly corresponds to the point at which the pulse intensity is half its maximum value: $t/\tau \approx -0.5$. Due to the presence of the field, the X population couples to the A state (red and blue dashed lines). Plotted below (a) and (b) is the probability distribution over the bend angle θ for the mixture of states displayed above, shown separately for (c) the case of a 10-fs pulse (blue) and (d) the case of a 40-fs pulse (red). In each case, dotted gray lines denote the equilibrium bend angles for the X and A states. In all four panels, green shading roughly indicates the window in time over which the second ionization event in sequential double-ionization is expected to occur.

where ω_0 is the carrier frequency, \mathcal{F}_0 is the peak electric field magnitude, and τ is the full width at half maximum of the corresponding intensity envelope $|F(t)|^2$.

The effects of the dipole coupling on the Wigner functions can be seen in Figs. 5(d)-5(g), while a more complete picture of the laser-driven dynamics is shown in Fig. 6. We first consider the Wigner functions. Figures 5(d) and 5(e) plot the Wigner functions on the X and A states, respectively, after the system was initialized with the Franck-Condon wave packet on the X state at the peak (t = 0) of a laser pulse with τ = 10 fs and an intensity of 400 TW/cm² and allowed to propagate for two cycles of the laser. Initially, only the X state is populated, but due to the near-resonant dipole coupling some population is transferred to the A state, which is discussed further below. In addition to the modifications due to field-free propagation, seen in Figs. 5(b) and 5(c), both of the Wigner functions on the X and A states have acquired additional structures after the laser-driven propagation. These structures arise due to light-induced potentials created by

the strong near-resonant laser field that modify the field-free potential-energy surfaces, an effect known as bond softening [60,61]. Additionally, the transfer of population from one state back to the other, which occurs through cascaded one-photon transitions between the X and A states induced by the strong near-resonant laser, also contributes to these structures. Figures S(f) and S(g) plot Wigner functions for the same scenario but now with the initial population starting on the A state. Again, it is seen that new structures not present in the Franck-Condon wave packet have developed.

For the permanent dipole moment effect on the nuclear dynamics simulation, a simple simulation was carried out, and negligible change in the simulated dynamics was seen. Other nonadiabatic or non-Born-Oppenheimer couplings, like the non-laser-induced nonadiabatic couplings, are also considered. The assumption in our calculations is that these couplings are negligible, so they are not included. These nonadiabatic couplings were also neglected in the classical trajectory simulations, so the two simulation sections (Secs. III and V) in the paper are consistent in this regard. More specifically, in the classical trajectories, they were performed field free and sampled from the Wigner distribution of the initial ground state. No nonadiabatic coupling between the nine potential surfaces was included, nor was coupling to other states that have conical intersections with some of these states which occur at geometries that are not probed by the classical trajectories. These points are discussed in [25,49]. Both of these previous works also neglected nonadiabatic transitions in the dissociation dynamics of the water dication. Comparison with experiment for one-photon double ionization verifies that nondiabatic effects do not appreciably change the final momentum distributions in the channels producing O/D⁺/D⁺ or OD⁺/D⁺. However, those effects can be important for the production of the products O⁺/D⁺/D, which are beyond the scope of this work.

In order to put things into perspective, we compare the amount of X to A coupling that occurs in a 10-fs pulse to a significantly longer pulse with a duration of 40 fs. Figure 6 shows a broader picture of the laser-driven dynamics. Figures 6(a) and 6(b) show the population of ground and first excited states of the monocation together with the laser field as a function of time for 10-fs and 40-fs laser pulses, respectively. Figures 6(c) and 6(d) show the corresponding probability density as a function of D-O-D angle and time. Figure 6 illustrates the fact that while population transfer and nuclear dynamics can take place during a 10-fs pulse, they have a much more dramatic effect for a 40-fs pulse.

The calculations described above suggest that in a longer pulse, dynamics in the monocation en route to the dication during a longer pulse also leads to significant unbending and a β -KER plot that is shifted to larger angles. We therefore compare the β -KER plot for 10- and 40-fs pulses as a test of the conclusions of the theoretical results. Figure 7 shows this comparison, which bears out the predictions based on the calculations above. We note that the comparison shows that 40-fs pulses tend to have larger β angles and also lower KER. The former is what we expected from the simulation, while the latter is not easy to explain. Nevertheless, this comparison provides strong evidence that while there is rough agreement between the measured and calculated momentum-resolved

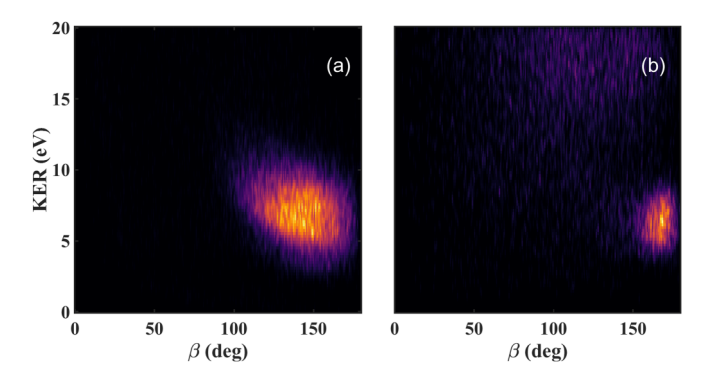


FIG. 7. β -KER plot for SFI with (a) 10-fs and (b) 40-fs pulse durations. A higher-kinetic-energy feature is observed for the longer pulses in (b). This feature can be assigned to trication formation and fragmentation via the D⁺/D⁺/O⁺channel, a discussion of which is presented in Appendix C.

fragment ion yields for sub-10-fs pulses assuming vertical ionization, reshaping of the wave packet and nuclear dynamics during ionization can lead to significant differences between strong- and weak-field ionizations. One needs to understand the strong-field dynamics in order to predict the reaction products in an SFI measurement. Finally, a weak diffuse feature at higher KER (\sim 20 eV) and smaller β values is observed for 40-fs pulses which is notably absent for the short-pulse case. This feature can readily be assigned to trication Coulomb explosion and is discussed in detail in Appendix C.

VI. CONCLUSION

In conclusion, while we found rough agreement between measurements of the $D^+/D^+/O$ yield as a function of β and KER for double ionization of D₂O with 10-fs laser pulses and calculations of the same yield assuming weak-field and vertical ionization, there are significant differences in the details. Even after careful analysis of the state population in the strong-field ionization and taking into account our experimental resolution, the experimental results still show discrepancies compared with theoretical expectations. As summarized in Fig. 8, these differences may be ascribed to different physical processes leading to wave-packet reshaping. The R-dependent single and double ionization induced by strong-field ionization and nuclear dynamics induced by resonance coupling during the pulse are believed to drive the wave packet away from the initial form. Such modifications to the wave function have great influence on the initial conditions of the trajectory calculations on dicationic states. Thus, the final experimental β -KER yield is different from the theoretical predictions from the simple single-photon double ionization. These effects in different physical processes result in SFI being a nonvertical transition, with an understanding of the strong-field dynamics being important for the calculation of the fragment-ion-yield momentum distributions.

Our simple calculations indicated that the coordinate dependence of the tunnel ionization rate plays an important role in reshaping the initial wave packet, particularly for the second ionization step in a sequential double-ionization process. Meanwhile, the simulated monocation dynamics in

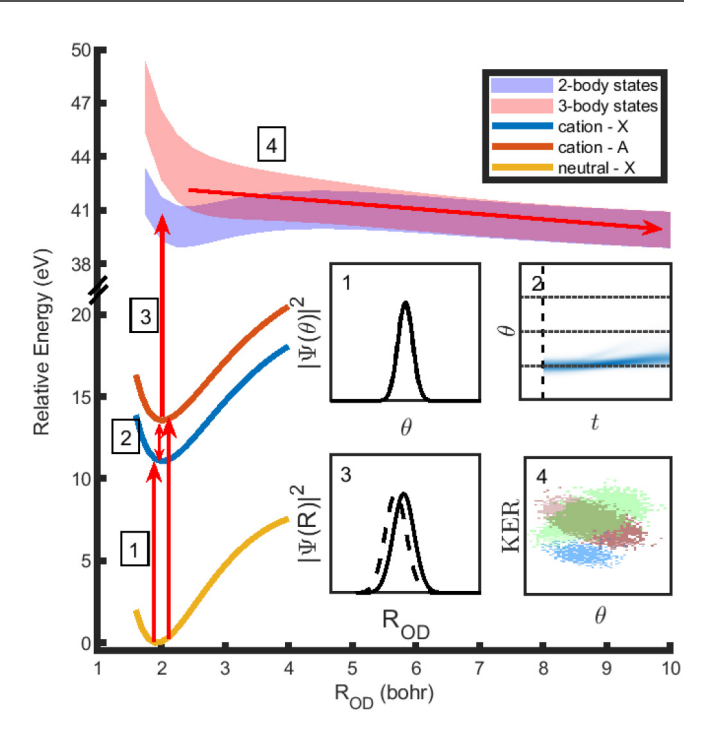


FIG. 8. Summary plot with PES of relevant states. From high energy to low energy are three-body dissociation states [red (light gray) shading], two-body dissociation states [magenta (dark gray) shading], the cationic *A* state [brown (medium gray) curve], the cationic *X* state [blue (dark gray) curve], and neutral *X* state [yellow (light gray) curve]. The four inset panels replotting the early figures (Figs. 3, 4, and 6). Four different steps participate in the strong-field double ionization of water: (1) tunnel ionization to the *X* and *A* states of the monocation, which involves reshaping of the wave function due to *R*-dependent ionization, (2) near-resonant coupling of *X* and *A* states as well as motion on the *A* state potential, (3) ionization to the dication, which also involves reshaping of the wave function, and (4) dication dissociation, which can be simulated through trajectory calculations.

the presence of the strong laser field indicated that field-dressed nuclear dynamics can also reshape the vibrational wave packet. These observations were supported by measurements of the double-ionization yield as a function of β and KER for 10- and 40-fs pulses. This comparison has significant bearing on the use of SFI as a probe of molecular structure and dynamics, and indicates that while very short pulses (<10 fs) can minimize nuclear dynamics during the pulse, wave-packet reshaping by the strong field of the laser can still result in significant distortion of the initial wave function of the molecule. We believe this work will have important consequences for pump-probe techniques, such as time-resolved Coulomb-explosion imaging, that aim to track nuclear dynamics during excited-state photochemical processes.

These results showcase the need for a more comprehensive theoretical description of SFI processes, which include the role of nuclear motion occurring during the ionizing laser pulse duration. As outlined in the Introduction, such nuclear dynamics could have implications for computations of SFI from multicycle pulses when invoking the frozen-nuclei approximation, such as recent state-of-the-art time-dependent *R*-matrix ionization computations for H₂O that highlighted

modifications to the angular dependence of ionization when significant laser coupling in the ion is present for the frozen-nuclei case. Further experimental investigations into the pulse shape and intensity dependence of SFI processes in water may help to target future modeling of these dynamics.

ACKNOWLEDGMENTS

We would like to thank B. M. Kaufman and Y. Liu for technical support and S. Matsika and J. Cryan for useful discussions. R.F., A.J.H., and P.H.B. were supported by the National Science Foundation. A.J.H. was additionally supported by a Stanford Graduate Fellowship as the 2019 Albion Walter Hewlett Fellow. C.C. and T.W. gratefully acknowledge support from the Department of Energy under Award No. DE-FG02-08ER15984. Work at Lawrence Berkeley National Laboratory (LBNL) was performed under the auspices of the U.S. Department of Energy (DOE), Office of Science, Office of Basic Energy Sciences, Chemical Sciences, Geosciences, and Biosciences Division under Contract No. DEAC02-05CH11231, using the National Energy Research Computing Center (NERSC), a DOE Office of Science User Facility, and the Lawrencium computational cluster resource provided by LBNL.

APPENDIX A: INDIVIDUAL DICATION-STATE CONTRIBUTIONS TO THE β -KER PLOT

In order to try to connect the observed dissociation features in our strong-field double-ionization experiment to specific dication states we adopted a methodology similar to that of Refs. [25,26]. In those studies, the $\rm H^+/H^+/O$ yield following single-photon double ionization of $\rm H_2O$ were compared against classical trajectory simulations on various electronic states of water diction. By comparing theoretical kinetic-energy releases (KERs) and relative angle correlations (between the two $\rm H^+$ fragments) to the experimental data, it was unambiguously shown that specific features could be connected to dissociation occurring on different electronic states of the dication.

Classical trajectory simulations of three-body dissociation of D_2O^{2+} into $D^+/D^+/O$ were performed using a methodology briefly outlined in Sec. III. In Fig. 3 theoretical KERs and D^+/D^+ relative angles β from these calculations are shown alongside the experimental data. In order to connect the features observed in theory to the dication states that are expected to undergo three-body decay (see Table II), Fig. 9 shows the β -KER plot with annotated regions corresponding to specific final states. For clarity we adopt the same state-specific color scheme as in Fig. 3.

APPENDIX B: ALTERNATIVE REPRESENTATIONS OF THE $D^+/D^+/O$ CHANNEL

Section II briefly outlined that by exploiting the Timepix3 camera in conjunction with a voltage-switching VMI apparatus it is possible to coincidentally detect all charge particles (electrons and ions) following strong-field double ionization, provided a suitably low number (\ll 1) of double-ionization events per laser shot is achieved. For the ions, the

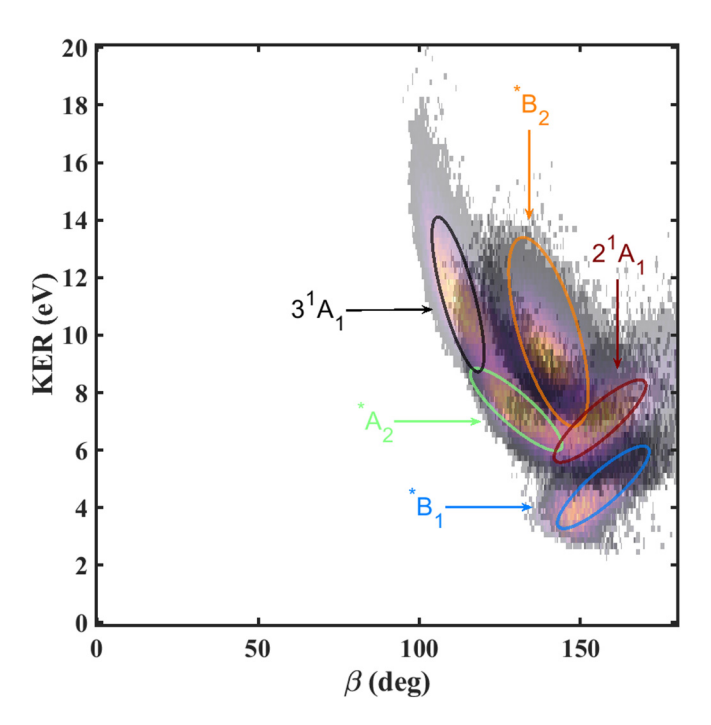


FIG. 9. Transparent theoretical β -KER plot generated from the simulations outlined in Sec. III. Annotations of the specific states associated with each distinct spectral feature are shown (ovals). State-dependent color coding consistent with Fig. 3 is adopted for clarity.

time-stamping capabilities of the camera permit the threedimensional vector momenta of all fragments to be extracted. This information permits observables, such as the relative angles between fragments or total KERs, to be determined. As outlined in the main text and Appendix A, a particularly useful way to view the data associated with the $D^+/D^+/O$ channel is to consider the relative angle between the two D⁺ ions β as a function of KER. We note, however, that there exists a large number of possible representations of the data due to three-dimensional correlated information extracted during the experiment. To highlight this, Fig. 10 shows various cuts of the full data set along the KER, β , E_{D1} , and E_{share} coordinates. Here E_{D1} and E_{share} refer to the kinetic energy of one of the deuterons and the sharing of kinetic energy between both deuterons, respectively. In Fig. 11 the equivalent plots for the theoretical simulations outlined in Sec. III are presented.

Similar to the discussion of the β -KER plot in the main text there exists some coarse agreement between theory and experiment in several of the panels. However, it is apparent that the well-resolved features in Fig. 11 are absent in the experimental data. This absence is likely due to the mechanisms outlined in Sec. V. A particularly noteworthy region of disagreement is observed in the panel where the yield is plotted as a function of E_{share} and β . A weak feature extending over all angles at $E_{\text{share}} = 0$ and 1 is seen experimentally but has no analogous signature in the theory. In Fig. 12 a zoomedin β - E_{share} plot is presented to highlight this discrepancy. We attribute this large angular spread in β to a process by which D_2O^{2+} initially undergoes two-body decay into D^+/OD^+ but subsequently fragments into three bodies $(D^+/D^+/O)$ via a

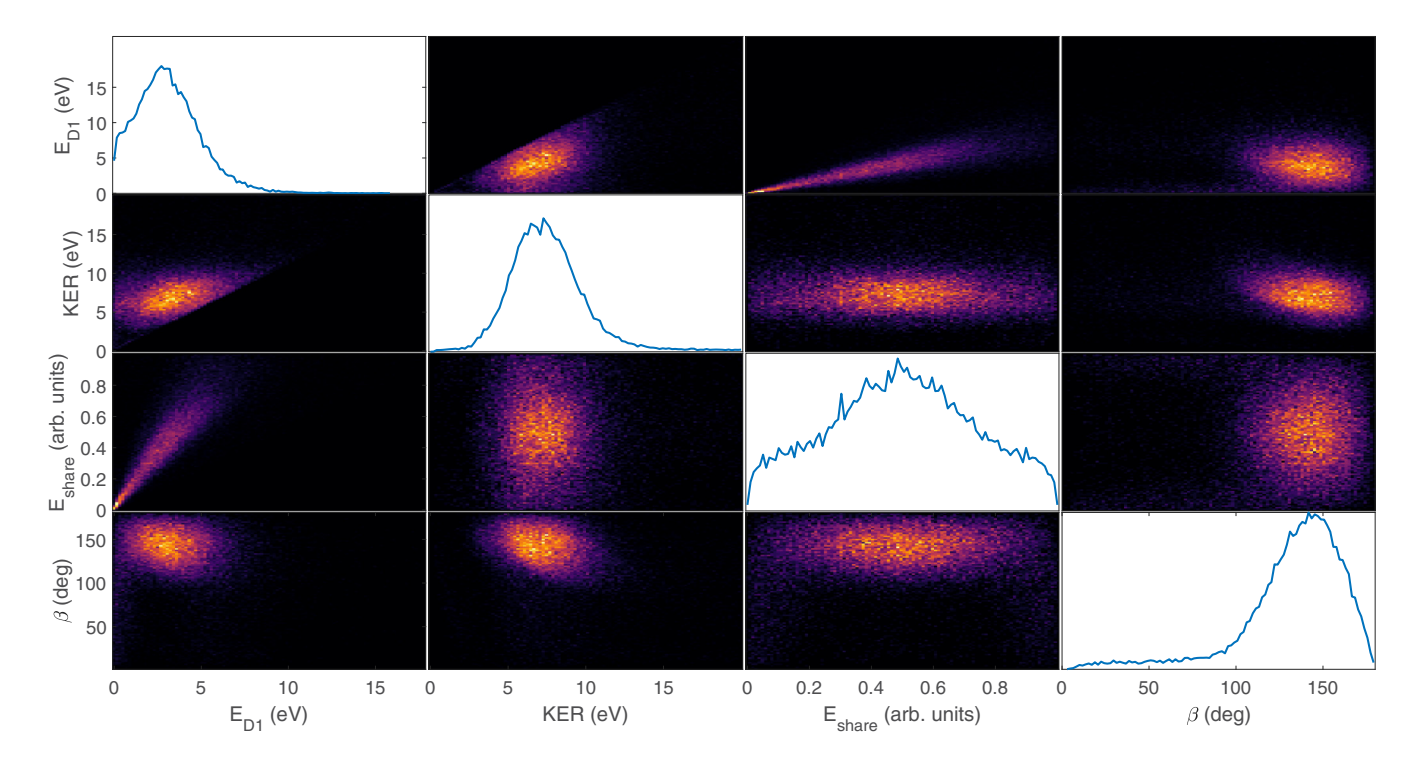


FIG. 10. Representations of the multidimensional $D^+/D^+/O$ coincidence data along various coordinates. Shown are KER, β , E_{D1} , and E_{share} cuts of the data along each of these coordinates in a matrix-style plot. Here the diagonal represents the one-dimensional normalized line-out along each of the aforementioned axes.

sequential breakup mechanism. A corresponding feature was observed in the $\rm H^+/H^+/O$ yield following single-photon double ionization [26] and has also been observed in SFI-induced fragmentation of triatomic molecules such as OCS [62].

APPENDIX C: SIGNATURES OF TRICATION FORMATION IN 40-FS PULSE DATA

The comparison of the β -KER plot for the cases of short (10 fs) and long (40 fs) pulse durations (see Fig. 7)

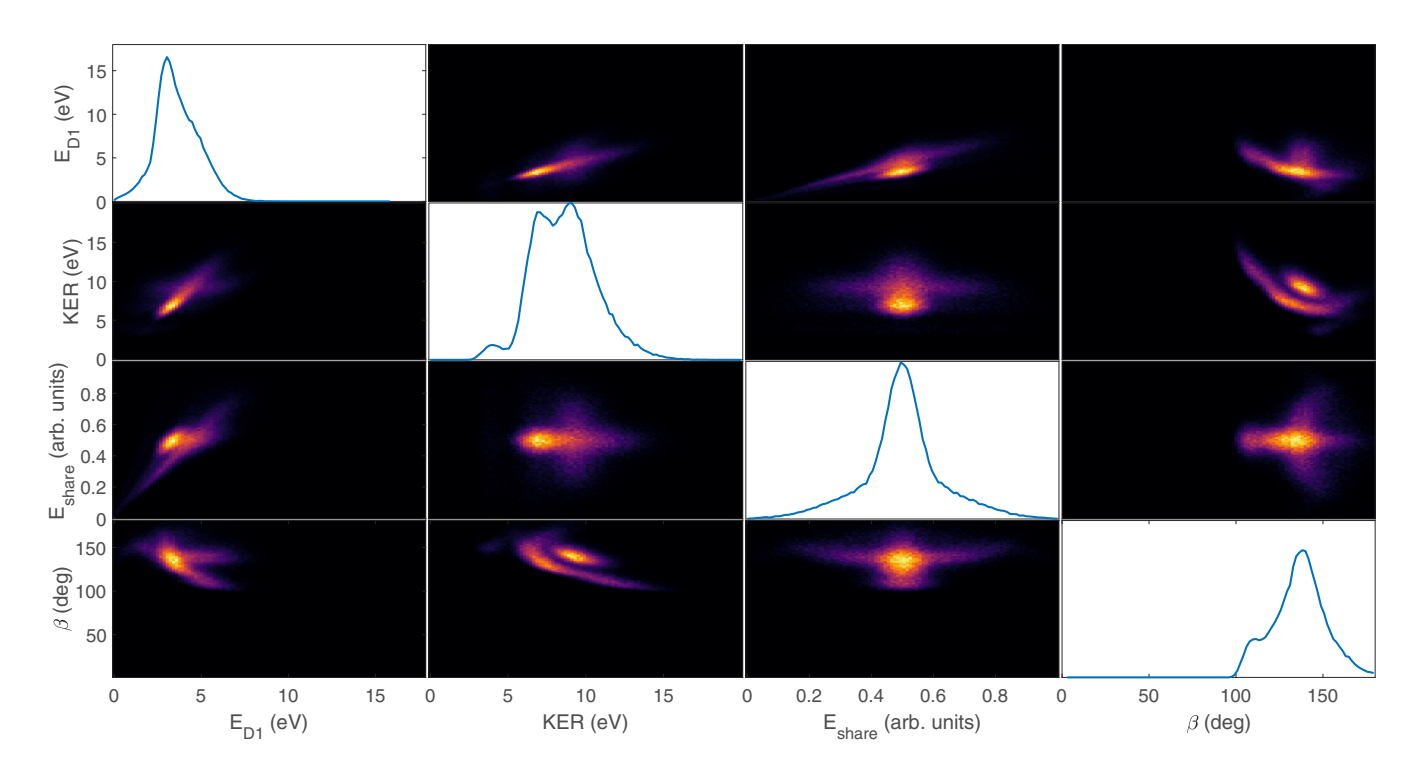


FIG. 11. Cuts of theoretical results along the same coordinates outlined in Fig. 10 for the $D^+/D^+/O$ fragmentation channel in the classical trajectory simulations. Details of constraints used to classify the trajectories into specific channels are outlined in Sec. III.

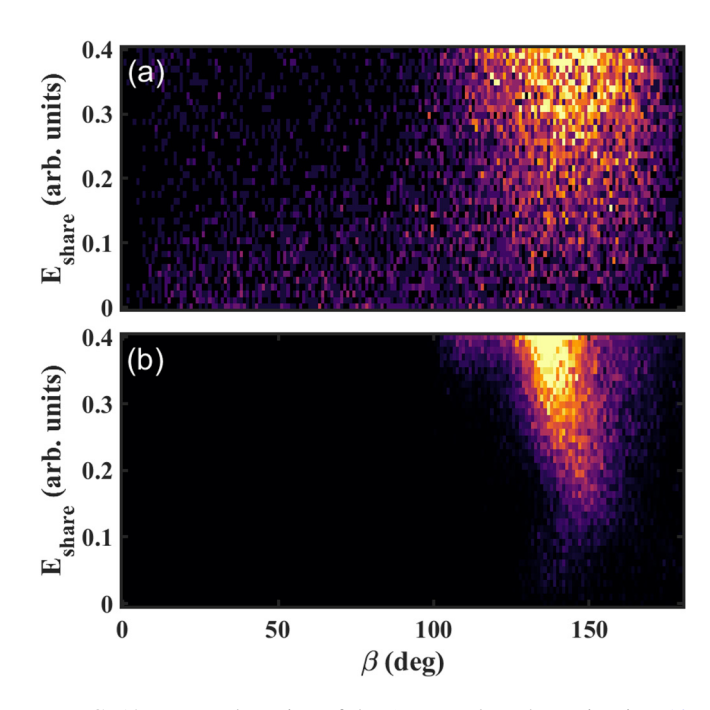


FIG. 12. Zoomed version of the β - $E_{\rm share}$ plots shown in Figs. 10 and 11. A broad feature in angle is observed at $E_{\rm share} < 0.2$ experimentally in (a), which is notably absent in the theoretical results in (b). This feature can be assigned to a sequential dissociation pathway involving predissociation of OD⁺, as discussed in the main text.

provided experimental support for the role of nuclear motion occurring during the double-ionization process. These data highlighted two significant differences. The first is a shifting of the feature observed at \sim 7.5 eV to higher β angles. This shift, as discussed in the main text, can be attributed to unbending dynamics that result in the water dication undergoing fragmentation from geometries close to linear. A second, higher-KER feature is discernible in the 40-fs data but is notably absent for the case of shorter pulses.

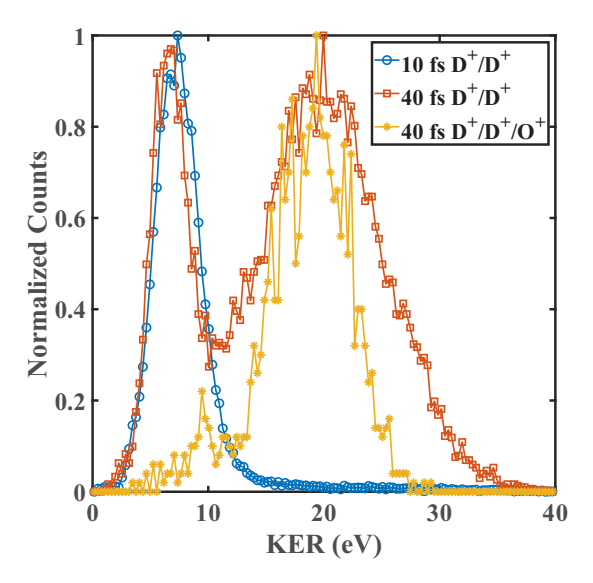


FIG. 13. KER distribution of the D^+/D^+ dissociation channel for 10-fs (blue circles) and 40-fs pulse durations (red squares) and $D^+/D^+/O^+$ for only the 40-fs pulse (yellow stars). The two D^+/D^+ line-outs correspond to β -angle-integrated versions of the data shown in Fig. 7. The overlap between the $D^+/D^+/O^+$ channel and D^+/D^+ in the 40-fs data indicates the high-KER region comes from events missing an O^+ .

In Fig. 13 we present β -angle-integrated KER spectra for the two pulse durations. A striking difference is observed between the spectra, with the majority of the 40-fs counts originating from the feature centered at \sim 20 eV. Given the significantly higher KER, a likely origin of this is fragmentation occurring from a more highly charged water ion and a missing coincidence partner ion (due to the limited detection efficiency of our apparatus). In order to verify this, we examined the $D^+/D^+/O^+$ coincidence channel and can unambiguously assign the origin of the higher-KER feature to such a process.

^[1] P.-M. Paul, E. S. Toma, P. Breger, G. Mullot, F. Augé, P. Balcou, H. G. Muller, and P. Agostini, Observation of a train of attosecond pulses from high harmonic generation, Science **292**, 1689 (2001).

^[2] T. Popmintchev, M.-C. Chen, D. Popmintchev, P. Arpin, S. Brown, S. Ališauskas, G. Andriukaitis, T. Balčiunas, O. D. Mücke, A. Pugzlys, A. Baltuška, B. Shim, S. E. Schrauth, A. Gaeta, C. Hernández-García, L. Plaja, A. Becker, A. Jaron-Becker, M. M. Murnane, and H. C. Kapteyn, Bright coherent ultrahigh harmonics in the keV X-ray regime from mid-infrared femtosecond lasers, Science 336, 1287 (2012).

^[3] J. Marangos, Development of high harmonic generation spectroscopy of organic molecules and biomolecules, J. Phys. B 49, 132001 (2016).

^[4] M. Meckel, D. Comtois, D. Zeidler, A. Staudte, D. Pavičić, H. Bandulet, H. Pépin, J. Kieffer, R. Dörner, D. Villeneuve *et al.*, Laser-induced electron tunneling and diffraction, Science 320, 1478 (2008).

^[5] K. Amini, M. Sclafani, T. Steinle, A.-T. Le, A. Sanchez, C. Müller, J. Steinmetzer, L. Yue, J. R. M. Saavedra, M. Hemmer et al., Imaging the Renner–Teller effect using laser-induced electron diffraction, Proc. Natl. Acad. Sci. USA 116, 8173 (2019).

^[6] C. I. Blaga, J. Xu, A. D. DiChiara, E. Sistrunk, K. Zhang, P. Agostini, T. A. Miller, L. F. DiMauro, and C. Lin, Imaging ultrafast molecular dynamics with laser-induced electron diffraction, Nature (London) 483, 194 (2012).

^[7] H. Stapelfeldt, E. Constant, H. Sakai, and P. B. Corkum, Timeresolved Coulomb explosion imaging: A method to measure structure and dynamics of molecular nuclear wave packets, Phys. Rev. A 58, 426 (1998).

^[8] I. Bocharova, R. Karimi, E. F. Penka, J.-P. Brichta, P. Lassonde, X. Fu, J.-C. Kieffer, A. D. Bandrauk, I. Litvinyuk, J. Sanderson, and F. Légaré, Charge Resonance Enhanced Ionization of CO₂ Probed by Laser Coulomb Explosion Imaging, Phys. Rev. Lett. 107, 063201 (2011).

- [9] P. M. Kraus, B. Mignolet, D. Baykusheva, A. Rupenyan, L. Horný, E. F. Penka, G. Grassi, O. I. Tolstikhin, J. Schneider, F. Jensen *et al.*, Measurement and laser control of attosecond charge migration in ionized iodoacetylene, Science 350, 790 (2015).
- [10] M. Kübel *et al.*, Steering Proton Migration in Hydrocarbons Using Intense Few-Cycle Laser Fields, Phys. Rev. Lett. 116, 193001 (2016).
- [11] M. Sabbar, H. Timmers, Y.-J. Chen, A. K. Pymer, Z.-H. Loh, S. G. Sayres, S. Pabst, R. Santra, and S. R. Leone, Stateresolved attosecond reversible and irreversible dynamics in strong optical fields, Nat. Phys. 13, 472 (2017).
- [12] K. Ramasesha, S. R. Leone, and D. M. Neumark, Real-time probing of electron dynamics using attosecond time-resolved spectroscopy, Annu. Rev. Phys. Chem. 67, 41 (2016).
- [13] T. K. Kjeldsen and L. B. Madsen, Strong-field ionization of diatomic molecules and companion atoms: Strong-field approximation and tunneling theory including nuclear motion, Phys. Rev. A 71, 023411 (2005).
- [14] K. Lin, X. Jia, Z. Yu, F. He, J. Ma, H. Li, X. Gong, Q. Song, Q. Ji, W. Zhang, H. Li, P. Lu, H. Zeng, J. Chen, and J. Wu, Comparison Study of Strong-Field Ionization of Molecules and Atoms by Bicircular Two-Color Femtosecond Laser Pulses, Phys. Rev. Lett. 119, 203202 (2017).
- [15] M. Lezius, V. Blanchet, D. M. Rayner, D. M. Villeneuve, A. Stolow, and M. Y. Ivanov, Nonadiabatic Multielectron Dynamics in Strong Field Molecular Ionization, Phys. Rev. Lett. 86, 51 (2001).
- [16] T. K. Kjeldsen, C. Z. Bisgaard, L. B. Madsen, and H. Stapelfeldt, Influence of molecular symmetry on strong-field ionization: Studies on ethylene, benzene, fluorobenzene, and chlorofluorobenzene, Phys. Rev. A 71, 013418 (2005).
- [17] L. Holmegaard, J. L. Hansen, L. Kalhøj, S. L. Kragh, H. Stapelfeldt, F. Filsinger, J. Küpper, G. Meijer, D. Dimitrovski, M. Abu-Samha *et al.*, Photoelectron angular distributions from strong-field ionization of oriented molecules, Nat. Phys. 6, 428 (2010).
- [18] F. Schell, A. E. Boguslavskiy, C. P. Schulz, S. Patchkovskii, M. J. Vrakking, A. Stolow, and J. Mikosch, Sequential and direct ionic excitation in the strong-field ionization of 1-butene molecules, Phys. Chem. Chem. Phys. 20, 14708 (2018).
- [19] P. Sándor, V. Tagliamonti, A. Zhao, T. Rozgonyi, M. Ruckenbauer, P. Marquetand, and T. Weinacht, Strong Field Molecular Ionization in the Impulsive Limit: Freezing Vibrations with Short Pulses, Phys. Rev. Lett. 116, 063002 (2016).
- [20] A. S. Coolidge, H. M. James, and R. D. Present, A study of the Franck-Condon principle, J. Chem. Phys. 4, 193 (1936).
- [21] X. Urbain, B. Fabre, E. M. Staicu-Casagrande, N. de Ruette, V. M. Andrianarijaona, J. Jureta, J. H. Posthumus, A. Saenz, E. Baldit, and C. Cornaggia, Intense-Laser-Field Ionization of Molecular Hydrogen in the Tunneling Regime and Its Effect on the Vibrational Excitation of H₂⁺, Phys. Rev. Lett. 92, 163004 (2004).
- [22] L. Fang and G. N. Gibson, Strong-Field Induced Vibrational Coherence in the Ground Electronic State of Hot I₂, Phys. Rev. Lett. **100**, 103003 (2008).
- [23] P. M. Kraus, S. B. Zhang, A. Gijsbertsen, R. R. Lucchese, N. Rohringer, and H. J. Wörner, High-Harmonic Probing of Electronic Coherence in Dynamically Aligned Molecules, Phys. Rev. Lett. 111, 243005 (2013).

- [24] Z. Liu, J. Yao, J. Chen, B. Xu, W. Chu, and Y. Cheng, Near-Resonant Raman Amplification in the Rotational Quantum Wave Packets of Nitrogen Molecular Ions Generated by Strong Field Ionization, Phys. Rev. Lett. 120, 083205 (2018).
- [25] Z. L. Streeter, F. L. Yip, R. R. Lucchese, B. Gervais, T. N. Rescigno, and C. W. McCurdy, Dissociation dynamics of the water dication following one-photon double ionization. I. Theory, Phys. Rev. A 98, 053429 (2018).
- [26] D. Reedy, J. B. Williams, B. Gaire, A. Gatton, M. Weller, A. Menssen, T. Bauer, K. Henrichs, Ph. Burzynski, B. Berry, Z. L. Streeter, J. Sartor, I. Ben-Itzhak, T. Jahnke, R. Dörner, T. Weber, and A. L. Landers, Dissociation dynamics of the water dication following one-photon double ionization. II. Experiment, Phys. Rev. A 98, 053430 (2018).
- [27] S. L. Horton, Y. Liu, P. Chakraborty, P. Marquetand, T. Rozgonyi, S. Matsika, and T. Weinacht, Strong-field-versus weak-field-ionization pump-probe spectroscopy, Phys. Rev. A 98, 053416 (2018).
- [28] R. Forbes, A. E. Boguslavskiy, I. Wilkinson, J. G. Underwood, and A. Stolow, Excited state wavepacket dynamics in NO₂ probed by strong-field ionization, J. Chem. Phys. 147, 054305 (2017).
- [29] X. Ding, R. Forbes, M. Kbel, K. F. Lee, M. Spanner, A. Y. Naumov, D. M. Villeneuve, A. Stolow, P. B. Corkum, and A. Staudte, Threshold photodissociation dynamics of NO₂ studied by time-resolved cold target recoil ion momentum spectroscopy, J. Chem. Phys. 151, 174301 (2019).
- [30] C. Petersen, E. Peronne, J. Thøgersen, H. Stapelfeldt, and M. Machholm, Control and imaging of interfering wave packets in dissociating I₂ molecules, Phys. Rev. A 70, 033404 (2004).
- [31] F. Légaré, K. F. Lee, I. V. Litvinyuk, P. W. Dooley, S. S. Wesolowski, P. R. Bunker, P. Dombi, F. Krausz, A. D. Bandrauk, D. M. Villeneuve, and P. B. Corkum, Laser Coulomb-explosion imaging of small molecules, Phys. Rev. A 71, 013415 (2005).
- [32] H. Liu, M. Li, X. Xie, C. Wu, Y. Deng, C. Wu, Q. Gong and Y. Liu, Charge resonance enhanced multiple ionization of H₂O molecules in intense laser fields, Chin. Phys. Lett. 32, 063301 (2015).
- [33] G. A. McCracken and P. H. Bucksbaum, Ionization induced dynamic alignment of water, J. Chem. Phys. 152, 134308 (2020).
- [34] A. J. Howard, C. Cheng, R. Forbes, G. A. McCracken, W. H. Mills, V. Makhija, M. Spanner, T. Weinacht, and P. H. Bucksbaum, Strong-field ionization of water: Nuclear dynamics revealed by varying the pulse duration, Phys. Rev. A 103, 043120 (2021).
- [35] S. Koh, K. Yamazaki, M. Kanno, H. Kono, and K. Yamanouchi, Ionization and dissociation dynamics of H₂O in ultrashort intense near-IR laser fields by the time-dependent adiabatic state method and the time-dependent configuration interaction method, Chem. Phys. Lett. 742, 137165 (2020).
- [36] C. Cheng, R. Forbes, A. J. Howard, M. Spanner, P. H. Bucksbaum, and T. Weinacht, Momentum-resolved above-threshold ionization of deuterated water, Phys. Rev. A 102, 052813 (2020).
- [37] J. Benda, J. D. Gorfinkiel, Z. Mašín, G. S. J. Armstrong, A. C. Brown, D. D. A. Clarke, H. W. van der Hart, and J. Wragg, Perturbative and nonperturbative photoionization of H₂ and H₂O

- using the molecular *R*-matrix-with-time method, Phys. Rev. A **102**, 052826 (2020).
- [38] M. Richter, M. Lytova, F. Morales, S. Haessler, O. Smirnova, M. Spanner, and M. Ivanov, Rotational quantum beat lasing without inversion, Optica 7, 586 (2020).
- [39] M. Lytova, M. Richter, F. Morales, O. Smirnova, M. Ivanov, and M. Spanner, N₂⁺ lasing: Gain and absorption in the presence of rotational coherence, Phys. Rev. A 102, 013111 (2020).
- [40] Q. Zhang, H. Xie, G. Li, X. Wang, H. Lei, J. Zhao, Z. Chen, J. Yao, Y. Cheng, and Z. Zhao, Sub-cycle coherent control of ionic dynamics via transient ionization injection, Commun. Phys. 3, 50 (2020).
- [41] A. Zhao, M. van Beuzekom, B. Bouwens, D. Byelov, I. Chakaberia, C. Cheng, E. Maddox, A. Nomerotski, P. Svihra, J. Visser *et al.*, Coincidence velocity map imaging using Tpx3Cam, a time stamping optical camera with 1.5 ns timing resolution, Rev. Sci. Instrum. 88, 113104 (2017).
- [42] C. Cheng, P. Vindel-Zandbergen, S. Matsika, and T. Weinacht, Electron correlation in channel-resolved strong-field molecular double ionization, Phys. Rev. A 100, 053405 (2019).
- [43] M. A. Dugan, J. X. Tull, and W. S. Warren, High-resolution acousto-optic shaping of unamplified and amplified femtosecond laser pulses, J. Opt. Soc. Am. B 14, 2348 (1997).
- [44] P. B. Corkum, Plasma Perspective on Strong Field Multiphoton Ionization, Phys. Rev. Lett. 71, 1994 (1993).
- [45] W. Bryan, S. Stebbings, J. McKenna, E. English, M. Suresh, J. Wood, B. Srigengan, I. Turcu, J. Smith, E. Divall *et al.*, Atomic excitation during recollision-free ultrafast multi-electron tunnel ionization, Nat. Phys. 2, 379 (2006).
- [46] O. Jagutzki, A. Cerezo, A. Czasch, R. Dorner, M. Hattas, Min Huang, V. Mergel, U. Spillmann, K. Ullmann-Pfleger, T. Weber, H. Schmidt-Bocking, and G. D. W. Smith, Multiple hit readout of a microchannel plate detector with a three-layer delay-line anode, IEEE Trans. Nucl. Sci. 49, 2477 (2002).
- [47] H. B. Pedersen, C. Domesle, L. Lammich, S. Dziarzhytski, N. Guerassimova, R. Treusch, L. S. Harbo, O. Heber, B. Jordon-Thaden, T. Arion, M. Förstel, M. Stier, U. Hergenhahn, and A. Wolf, Photolysis of water-radical ions H₂O⁺ in the XUV: Fragmentation through dicationic states, Phys. Rev. A 87, 013402 (2013).
- [48] S. Zhao, B. Jochim, P. Feizollah, J. Rajput, F. Ziaee, K. Raju P., B. Kaderiya, K. Borne, Y. Malakar, B. Berry, J. Harrington, D. Rolles, A. Rudenko, K. D. Carnes, E. Wells, I. Ben-Itzhak, and T. Severt, Strong-field-induced bond rearrangement in triatomic molecules, Phys. Rev. A 99, 053412 (2019).

- [49] B. Gervais, E. Giglio, L. Adoui, A. Cassimi, D. Duflot, and M. Galassi, The H₂O²⁺ potential energy surfaces dissociating into H⁺/OH⁺: Theoretical analysis of the isotopic effect, J. Chem. Phys. **131**, 024302 (2009).
- [50] H.-J. Werner, P. J. Knowles, G. Knizia, F. R. Manby, and M. Schütz, MOLPRO: A general-purpose quantum chemistry program package, Wiley Interdiscip. Rev.: Comput. Mol. Sci. 2, 242 (2012).
- [51] H.-J. Werner, P. J. Knowles, G. Knizia, F. R. Manby, M. Schütz et al., MOLPRO, version 2015.1, a package of ab initio programs, http://www.molpro.net.
- [52] J. Ullrich, R. Moshammer, R. Dörner, O. Jagutzki, V. Mergel, H. Schmidt-Böcking, and L. Spielberger, Recoil-ion momentum spectroscopy, J. Phys. B 30, 2917 (1997).
- [53] R. Dörner, V. Mergel, O. Jagutzki, L. Spielberger, J. Ullrich, R. Moshammer, and H. Schmidt-Böcking, Cold target recoil ion momentum spectroscopy: A 'momentum microscope' to view atomic collision dynamics, Phys. Rep. 330, 95 (2000).
- [54] J. Ullrich, R. Moshammer, A. Dorn, R. Dörner, L. P. H. Schmidt, and H. Schmidt-Böcking, Recoil-ion and electron momentum spectroscopy: Reaction-microscopes, Rep. Prog. Phys. 66, 1463 (2003).
- [55] X.-M. Tong, Z. X. Zhao, and C.-D. Lin, Theory of molecular tunneling ionization, Phys. Rev. A 66, 033402 (2002).
- [56] L. Keldysh *et al.*, Ionization in the field of a strong electromagnetic wave, Sov. Phys. JETP 20, 1307 (1965).
- [57] A. Saenz, Enhanced ionization of molecular hydrogen in very strong fields, Phys. Rev. A 61, 051402 (2000).
- [58] A. Perelomov, V. Popov, and M. Terentev, Ionization of atoms in an alternating electric field, Sov. Phys. JETP **23**, 924 (1966).
- [59] M. Feit, J. Fleck, and A. Steiger, Solution of the Schrödinger equation by a spectral method, J. Comput. Phys. 47, 412 (1982).
- [60] P. H. Bucksbaum, A. Zavriyev, H. G. Muller, and D. W. Schumacher, Softening of the H₂⁺ Molecular Bond in Intense Laser Fields, Phys. Rev. Lett. 64, 1883 (1990).
- [61] J. H. Sanderson, A. El-Zein, W. A. Bryan, W. R. Newell, A. J. Langley, and P. F. Taday, Geometry modifications and alignment of H_2O in an intense femtosecond laser pulse, Phys. Rev. A **59**, R2567 (1999).
- [62] J. Rajput, T. Severt, B. Berry, B. Jochim, P. Feizollah, B. Kaderiya, M. Zohrabi, U. Ablikim, F. Ziaee, K. Raju P., D. Rolles, A. Rudenko, K. D. Carnes, B. D. Esry, and I. Ben-Itzhak, Native Frames: Disentangling Sequential from Concerted Three-Body Fragmentation, Phys. Rev. Lett. 120, 103001 (2018).